Synthesis, structure, and polymorphic transitions of praseodymium(iii) and neodymium(iii) borohydride, Pr(BH4)3and Nd(BH4)3

Synthesis, Structure, and Polymorphic Transitions of Praseodymium(III) and Neodymium(III) Borohydride, $Pr(BH_4)_3$ and $Nd(BH_4)_3$

SeyedHosein Payandeh GharibDoust[a]*, Michael Heere[b,c], Carlo Nervi[d], Magnus H. Sørby[b], Bjørn C. Hauback[b], Torben R. Jensen[a]*

[a]Center for Materials Crystallography, Interdisciplinary Nanoscience Center (iNANO) and Department of Chemistry, Aarhus University, Langelandsgade 140, DK-8000 Århus C, Denmark

[b]Physics Department, Institute for Energy Technology, NO-2027 Kjeller, Norway

[c]Research Neutron Source Munich (FRM2) and Karlsruhe Institute of Technology (KIT), Institute for Applied Materials—Energy Storage Systems (IAM-ESS), 76344 Eggenstein, Germany

[d]Department of Chemistry, NIS and CIRCC, University of Turin, Via P. Giuria 9, I-10125 Torino, Italy

*Corresponding Authors: (SHPGD) a.payande88@gmail.com; (TRJ) trj@chem.au.dk

ToC Figure

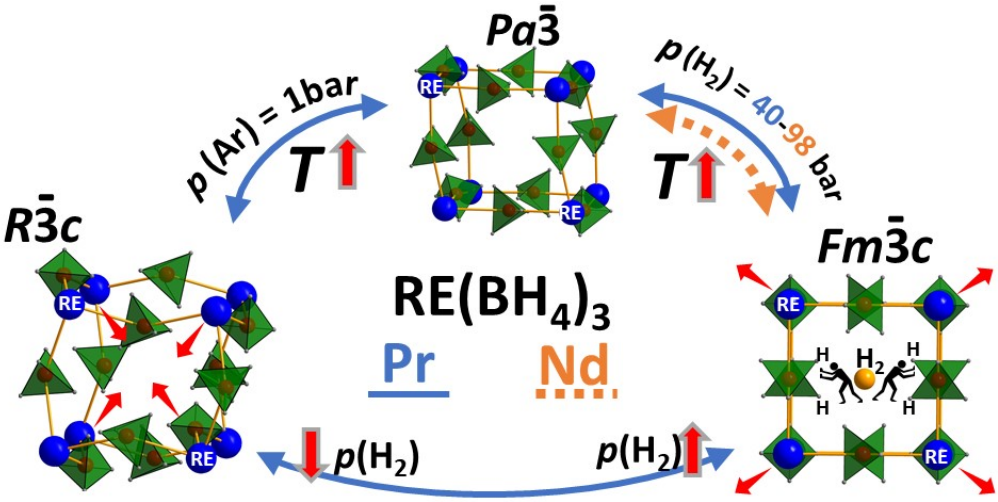

Abstract

In this work, praseodymium(III) borohydride, $Pr(BH_4)_3$, and the isotopically enriched analogue, $Pr(^{11}BD_4)_3$, are prepared by a new route via a solvate complex, $Pr(^{11}BD_4)_3S(CH_3)_2$. $Nd(BH_4)_3$ was synthesized using the same method and the structures, polymorphic transformations, and thermal stabilities of these compounds are investigated in detail. α-$Pr(BH_4)_3$ and α-$Nd(BH_4)_3$ are isostructural with cubic unit cells ($Pa\bar{3}$) stable at room temperature (RT) and unit cell volume per formula unit (V/Z) of 180.1 and 175.8 Å^3, respectively. Heating α-$Pr(BH_4)_3$ to $T \sim 190$ °C, p(Ar) = 1 bar, introduces a transition to a rhombohedral polymorph, r-$Pr(BH_4)_3$ ($R\bar{3}c$) with smaller unit cell volume and denser structure, V/Z = 156.06 Å^3. A similar transition was not observed for $Nd(BH_4)_3$. However, heat treatment of α-$Pr(BH_4)_3$, at $T \sim 190$ °C, $p(H_2)$ = 40 bar and α-$Nd(BH_4)_3$, at $T \sim 270$ °C, $p(H_2)$ = 98 bar facilitate reversible formation of another three cubic polymorph, denoted β, β'-$RE(BH_4)_3$ and β''-$RE(BH_4)_3$ ($Fm\bar{3}c$). Moreover, the transition β- to β'- to β''- is considered a rare example of stepwise negative thermal expansion. For $Pr(BH_4)_3$, ~2/3 of the sample take this route of transformation whereas in argon only ~5 wt%, and the remaining transforms directly from α- to r-$Pr(BH_4)_3$. The β-polymorphs are porous with V/Z = 172.4 and 172.7 Å^3 for β''-$RE(BH_4)_3$, RE = Pr or Nd, respectively, and are stabilized by the elevated hydrogen pressures. The polymorphic transitions occur due to rotation of $RE(BH_4)_6$ octahedra without breaking or forming chemical bonds. Structural DFT optimization reveals decreasing stability of α–$Pr(BH_4)_3$ > β–$Pr(BH_4)_3$ > r–$Pr(BH_4)_3$.

Introduction

One of the greatest challenges in the 21st century is the transition towards a sustainable and environmentally friendly energy system.[1,2] Hydrogen is the most abundant and lightest element and has the highest gravimetric energy density for any known substance. Hydrogen is therefore an ideal (renewable) energy carrier.[3–5] Metal borohydrides have received considerable attention as potential hydrogen storage materials due to their high hydrogen densities.[6,7] A wide variety of metal borohydrides have been synthesized and characterized, and an inverse correlation has been found between the decomposition temperature of the metal borohydride and the Pauling electronegativity of the metal.[7,8] In recent years, rare-earth (RE) metal borohydrides, in particular, have received considerable interest due to their various properties.[9–14] $RE(BH_4)_2(THF)_2$ (RE = Eu and Yb, THF = tetrahydrofuran) have shown high luminescent properties[15], and other lanthanide borohydride complexes such as $RE(BH_4)_3(THF)_3$ (RE = Nd, Sm) have been used extensively for the catalysis of organic polymerization reactions.[16–18] These compounds have a higher solubility in apolar solvents compared to that of traditional $RECl_3(THF)_3$ compounds, which makes them promising candidates as catalysts.[16–18] The hydrogen capacities of rare-earth metal borohydrides, $RE(BH_4)_n$, n = 2, 3, vary between 9.07 wt% H_2 for $Y(BH_4)_3$ to 5.56 wt% for $Yb(BH_4)_3$,[19–24] and is within the range of MgH_2 (7.65 wt% H_2) and $NaAlH_4$ (7.46 wt% H_2), which have previously received considerable attention.[25,26] Bimetallic rare-earth borohydrides such as $MY(BH_4)_4$, M = Li, Na, and $LiRE(BH_4)_3Cl$, RE = La, Ce, Gd have moderate to high Li and Na ion conductivity.[12,13,27–31] Magnetocaloric properties have also been observed for $K_2Gd(BH_4)_5$ and $Cs_3Gd(BH_4)_6$.[32]

The crystal chemistry of rare-earth metal borohydrides, $RE(BH_4)_3$, is diverse and interesting.[5,33] Metal borohydrides with the largest cations, RE = La, Ce, crystallize in the trigonal crystal system with space group $R\bar{3}c$ (*r*-$RE(BH_4)_3$).[13,34] Smaller cations, e.g. Pr to

Yb, crystallize in the cubic crystal system with space group $Pa\bar{3}$ (α-$RE(BH_4)_3$).[19,23,35] Most of the trivalent rare-earth borohydrides undergo a transition to a second cubic polymorph with space group symmetry either $Pm\bar{3}m$ or $Fm\bar{3}c$ at elevated temperatures (β-$RE(BH_4)_3$).[19,23,35–39] All known $RE(BH_4)_3$ with space group symmetry $Pa\bar{3}$, $R\bar{3}c$, $Pm\bar{3}m$, or $Fm\bar{3}c$ have crystal structures related to polymorphs of rhenium trioxide, ReO_3.[33,34] Some rare-earth metals form stable borohydrides in oxidation state (II), e.g. Sm^{2+} and Eu^{2+}, which crystallize in the orthorhombic crystal system (space group *Pbcn*) at RT. Upon heating, europium(II) borohydride, $Eu(BH_4)_2$, transforms into tetragonal and cubic polymorphs with space group symmetry $P4_12_12$ and $Fm\bar{3}m$, respectively.[21,24]

Previous methods for the synthesis of trivalent rare-earth metal borohydrides were based on the reaction of $LiBH_4$ with $RECl_3$,[23,34] but the products obtained using this method were contaminated with amorphous $LiBH_4$. The presence of amorphous $LiBH_4$ has consequences for thermal properties and chemical reactivity of samples prepared by this method. For example, $La(BH_4)_3$ synthesized according to this method formed $Li_3K_3La_2(BH_4)_{12}$ upon the reaction with KBH_4.[13] Therefore, our focus has been on new synthetic strategies and investigation of chemical, physical, and structural properties of the pure compounds. Here we present a new method to obtain solvate complexes, $RE(BH_4)_3S(CH_3)_2$, RE = Pr, Nd, and the corresponding borohydrides, $Pr(BH_4)_3$, $Nd(BH_4)_3$, which allows detailed investigation of the polymorphic transformations.

2. Experimental

2.1 Sample preparation

$Pr(BH_4)_3$ and $Nd(BH_4)_3$ compounds were synthesized using a new method based on the reaction of PrH_3 or NdH_3 with dimethyl sulfide borane complex, $S(CH_3)_2BH_3$ (DMS). RE metal ingots were scrapped with sand paper to remove the oxide layer, placed in an

autoclave, and heated up to 380 °C for 2 hours under hydrogen pressure $p(H_2)$ = 100 bar to form REH_3 (RE = Pr, Nd). The formation of REH_3 was confirmed by X-ray powder diffraction (XRPD). However, the hydrogenation was repeated for the second time in order to prevent contamination of the sample with RE metal. In the next step, the REH_3 (RE = Pr, Nd) powder was ball milled for two hours under argon atmosphere (10 min milling, 2 min break, 12 repetitions) and a powder-to-ball ratio of 1:20. A Fritsch Pulverisette 6 planetary ball mill was used, which was equipped with a tungsten carbide vial (80 mL) and balls (o.d. 10 mm).
The ball-milled powder was transferred to a reaction flask and mixed with $S(CH_3)_2BH_3$ in toluene solvent (10 M) in the molar ratio of 1:4.5. The excess of $S(CH_3)_2BH_3$ solvent was used to completely consume the REH_3, and the solution was diluted to half-concentration by adding the same volume of toluene. The mixture was stirred for 2 days at 45 °C. Then the temperature was decreased to 35 °C and dimethyl sulfide was added to the mixture (50 mL per gram of REH_3) in order to dissolve $RE(BH_4)_3S(CH_3)_2$, allowing the removal of possible remaining REH_3 in the sample. After one day of stirring at 35 °C, the solution was filtered, and the solvent was removed using a rotary evaporator at 70 °C.

At this stage, $RE(BH_4)_3S(CH_3)_2$ (RE = Pr, Nd) was obtained. In order to remove the coordinated solvent, the powder was transferred to a glass tube and annealed at 180 °C under vacuum for 1 h. The sample was then ground with mortar and pestle in the glovebox. The heat treatment was repeated once more in order to completely remove the DMS solvent from the sample.

An isotopically enriched sample of praseodymium(III) borohydride, $Pr(^{11}BD_4)_3$, was prepared using the same procedure with different reagents. For deuteration, the Pr ingots were transferred to an autoclave placed in liquid nitrogen and deuterium, D_2, gas was added ($p(D_2)$ = 8 bar) and the pressure increased to $p(D_2)$ = 14 bar upon heating to the autoclave room

temperature (RT). The autoclave was then heated further to 390 °C for 2 hours. The deuteration procedure was repeated three times in order to fully convert the Pr metal to PrD_3. The solvated praseodymium(III) borohydride was prepared using $S(CH_3)_2(^{11}BD_3)$ and with the same procedures as described above.

$LiBH_4$ (95%), toluene, $C_6H_5CH_3$ (anhydrous, 99.8%), dimethyl sulfide, DMS, $S(CH_3)_2$ (anhydrous, 99.9%), praseodymium, Pr (99.9%), and Neodymium, Nd (99.9%) ingots were purchased from Sigma-Aldrich. $S(CH_3)_2BH_3$ and $S(CH_3)_2{}^{11}BD_3$ (10.0 M in toluene) were purchased from Katchem. All chemicals were used as received and sample manipulation was performed in an argon-filled glove box with circulation purifier, (O_2, H_2O) < 0.5 ppm.

Table 1 Overview of investigated samples, molar ratio of the used reactants, synthesis procedure, and the sample composition determined by Rietveld refinement of XRPD/NPD data. * Rietveld refinement is based on NPD.

Sample	Reactants	Molar ratio	Preparation method	Products observed by XRPD/NPD (wt%)
s1	PrD_3 - $S(CH_3)_2{}^{11}BD_3$	1:4.5	Solvent method	$Pr(^{11}BD_4)_3S(CH_3)_2$, 91.1(9) α-$Pr(^{11}BD_4)_3$ - $Pa\bar{3}$, 7.4(2) β-$Pr(^{11}BD_4)_3$ - $Fm\bar{3}c$, 1.5(1)
s2	PrD_3 - $S(CH_3)_2{}^{11}BD_3$	1:4.5	Solvent method, T = 180 °C, 1 h	α-$Pr(^{11}BD_4)_3$ - $Pa\bar{3}$, 100.0 (1)*
s3	PrH_3 - $S(CH_3)_2BH_3$	1:4.5	Solvent method, T = 180 °C, 1 h	α-$Pr(BH_4)_3$ - $Pa\bar{3}$, 97.9(2) β-$Pr(BH_4)_3$ - $Fm\bar{3}c$, 3.1(3)
s4	NdH_3 - $S(CH_3)_2BH_3$	1:4.5	Solvent method	$Nd(BH_4)_3S(CH_3)_2$, 100.0 (1)
s5	NdH_3 - $S(CH_3)_2BH_3$	1:4.5	Solvent method, T = 180 °C, 1 h	α-$Nd(BH_4)_3$ - $Pa\bar{3}$, 93.2(1) β-$Nd(BH_4)_3$ - $Fm\bar{3}c$, 6.8(5)

2.2 *In-situ* Synchrotron Radiation X-ray Powder Diffraction

In-situ synchrotron radiation X-ray powder diffraction (SR-XRPD) data of the samples were collected at the Swiss–Norwegian Beam Line (SNBL, BM01A) at ESRF, Grenoble, France, and at the P02 beamline at Petra III, Desy, Hamburg, Germany. At SNBL, a Dexela–Perkin

Elmer 2923 CMOS pixel detector[40] was used, and the wavelength was 0.7129 Å. At Petra III, a PerkinElmer XRD1621 detector was used, and the selected X-ray wavelength was 0.2072 Å. The samples were mounted in boron silicate capillaries (o.d. 0.5 mm) under argon and sealed with glue to prevent contact with air. For the *in-situ* XRPD experiment under pressure which was performed in ESRF, the sample was loaded in a quartz capillary (o.d. 0.5 mm) and attached to a specially designed sample holder from ESRF, and hydrogen gas was applied, $p(H_2)$ = 40 bar. For the high-pressure experiments performed in the P02 beamline at Petra III, samples were packed in sapphire tubes (i.d. 0.8 mm), attached to a specially designed sample cell for studying solid-gas reactions, and hydrogen gas was applied, $p(H_2)$ = 98 bar.[41,42]

2.3 Neutron powder diffraction

Neutron powder diffraction (NPD) data of $Pr(^{11}BD_4)_3$ sample were collected at two different places, the spallation neutron source SINQ at the Paul Scherrer Institute in Villigen, Switzerland and the JEEP II reactor at Institute for Energy Technology in Kjeller, Norway. At SINQ, NPD data were collected at the high-resolution powder neutron diffractometer (HRPT) from 2θ = 10° to 130°.[43] The powder sample was enclosed in a vanadium can (8 mm diameter), and data were collected with a wavelength of λ = 1.494 Å. At JEEP II reactor data were collected using the PUS instrument and neutrons with λ = 1.5583 Å were obtained from a Ge (511) focusing monochromator. Data were collected from 10° to 130° in steps of 0.05° in 2θ.[44]

2.4 Structure solution and refinement

A new solvate compound and new polymorphs of $Pr(BH_4)_3$, rhombohedral *r*-$Pr(BH_4)_3$ ($R\bar{3}c$) and cubic β-$Pr(BH_4)_3$ ($Fm\bar{3}c$), were identified and structurally characterized in this investigation, see Table 2 and Tables S2, S3. Moreover, a new high-temperature polymorphs of $Nd(BH_4)_3$ ($Fm\bar{3}c$) were identified. Structural models for the new compounds were derived

from isostructural known compounds as discussed in the next sections. The structure models were refined using X-ray and neutron powder diffraction data with the Rietveld method implemented in the program Fullprof.[45] Data collected for samples **s1** were used to refine the structural models of $Pr(^{11}BD_4)_3S(CH_3)_2$ and *r*-$Pr(^{11}BD_4)_3$, resulting in R_{wp} = 6.43 and 4.66 % (not corrected for background), respectively (Figures **S7** and **S6**). In order to confirm the crystal structure of *r*-$Pr(BH_4)_3$, and to obtain the exact position of H atoms, $Pr(^{11}BD_4)_3$ was synthesized, and NPD of sample **s2** was used to refine the structure model with R_{wp} = 3.95 % (not corrected for background), χ^2 = 4.12 (Figure **S11**). Moreover, the crystal structure of $Pr(^{11}BD_4)_3S(CH_3)_2$ was confirmed by Rietveld refinement based on NPD data with R_{wp} = 2.00 % (not corrected for background), χ^2 = 2.18 (Figure **S9**). NPD data of $Pr(BD_4)_3S(CH_3)_2$ and *r*-$Pr(BD_4)_3$ were collected from 2θ 10° to 130°, however, Rietveld refinements of these structures were performed in the 2θ range of 10° to 110° and 10° to 70°, respectively. This was due to the low quality of the neutron diffraction data at high 2θ angles.

The crystal structure of β-$Pr(BH_4)_3$ and β-$Nd(BH_4)_3$ was refined based on the XRPD pattern of samples **s3** and **s5** resulting in R_{wp} = 2.22 % and 4.59 % and χ^2 = 301 and 5970, respectively (see Figures **S5** and **S12**). The high χ^2 value is due to extremely high counting statistics of the powder diffraction data obtained from modern 2D detectors. The crystal structures obtained by powder X-ray diffraction were refined based on the fixed positions of the elements in the (known) structure models. Therefore, H-H or D-D distances in these data were obtained by considering the original coordinates of the H/D atoms. The structural model of $Y(BH_4)_3$ that was used to refine the structure of the two polymorphs ($Pa\bar{3}$ and $Fm\bar{3}c$) had been optimized by DFT and the H/D coordinates are considered reliable.[37] The $R\bar{3}c$ structural model for $La(BH_4)_3$ was not optimized by DFT,[34] however, the original coordinates of the H/D atoms were used for refinement. In the next step, the H-H/ D-D distances were

compared to the refinement based on NPD data. In the NPD data refinement, the coordinates of D atoms were refined and for this purpose, additional strains were added to the structures, and B-D and D-D distances were fixed at 1.19 and 1.90 Å, respectively. The D-D distances obtained by NPD were in agreement with the values obtained by XRPD. The backgrounds were described by linear interpolation between selected points. Unit cell parameters, scale factors, zero-point, peak shape mixing parameters (pseudo-Voigt function), and three profile parameters (U, V, W) were refined. The crystallographic data of the compounds are provided in Table 2.

2.5 Thermal Analysis and Mass Spectrometry

The thermal behavior of the samples was studied by combined thermogravimetric analysis (TGA), differential scanning calorimetry (DSC), and mass spectrometry (MS). DSC and TGA were carried out using a PerkinElmer STA 6000 apparatus, which was attached to a Hiden Analytical HPR-20 QMS mass spectrometer. Approximately 10 mg of the sample was placed in an Al_2O_3 crucible and heated from 40 to 500 °C ($\Delta T/\Delta t$ = 5 °C min^{-1}) in an argon flow of 40 mL min^{-1}. The evolved gases were transported to MS and analyzed for H_2 (m/z = 2) and B_2H_6 (m/z = 27).

2.6 DFT Calculations

Quantum Espresso version 6.1,[46] was employed for DFT periodic lattice calculations using the Generalized Gradient Approximation (GGA) functional PW86PBE,[47,48] with the inclusion of the exchange-hole dipole moment (XDM) dispersion correction method[49,50] for modeling weak interactions. XDM dispersion energies were calculated adopting the damping parameters optimized for similar inorganic systems.[51] Cut-offs of 60 Ry were used for structural optimizations. The Brillouin zones were automatically sampled with the Monkhorst–Pack scheme[52] in a similar approach as previously described.[53] Geometry optimization was performed with a grid mesh of 1×1×2.

3. Result and discussion

3.1 Synthesis

A new approach to synthesize pure rare-earth metal borohydrides is presented using metal hydrides, REH_3, RE = Pr, Nd, and a borane donating complex, $S(CH_3)_2BH_3$ in solution, forming solvated complexes, see reaction scheme 1.

$$REH_3(s) + 3S(CH_3)_2BH_3(toluene) \rightarrow RE(BH_4)_3S(CH_3)_2(s) + 2S(CH_3)_2(toluene) \quad (1)$$

Using this method, $Pr(BH_4)_3S(CH_3)_2$ and $Nd(BH_4)_3S(CH_3)_2$ are synthesized and $Pr(BH_4)_3$ and $Nd(BH_4)_3$ are obtained by heating the solvate complexes in vacuum at 180 °C, see reaction scheme 2.

$$RE(BH_4)_3S(CH_3)_2(s) \rightarrow \alpha\text{-}RE(BH_4)_3(s) + S(CH_3)_2(g),\ RE = Pr, Nd \quad (2)$$

$Pr(^{11}BD_4)_3S(CH_3)_2$ and $Pr(^{11}BD_4)_3$ were synthesized using a similar approach, reaction 1 and 2, and PrD_3 and $S(CH_3)_2{}^{11}BD_3$ as reactants.

3.2. Structure analysis

3.2.1. Crystal structure of $RE(BH_4)_3S(CH_3)_2$, RE = Pr, Nd

The diffraction patterns of praseodymium(III) and neodymium(III) borohydride dimethyl sulfide complex, $RE(BH_4)_3S(CH_3)_2$, RE = Pr, Nd clearly resembled the Bragg reflections of $Y(BH_4)_3S(CH_3)_2$ and $Gd(BH_4)_3S(CH_3)_2$.[36] Therefore, the $Y(BH_4)_3S(CH_3)_2$ structure (monoclinic, $P2_1/c$) was used as an initial structural model for Rietveld refinements, see Table 2. In this structure, the rare-earth cation is coordinated to five BH_4^- units and a sulfur atom from the dimethyl sulfide molecule, forming a distorted octahedral geometry. Four BH_4^- groups are bridging between the RE^{3+} centers by edge sharing, bidentate (η^2) coordination, and the remaining BH_4^- group is a terminal ligand. The $S(CH_3)_2$ molecule coordinates to RE^{3+} via the S atom of $S(CH_3)_2$ (Figure 1). The structure of $Pr(^{11}BD_4)_3S(CH_3)_2$ was refined with

the Rietveld method using both X-ray and neutron powder diffraction data, see Figures S7 and S8. The refined structural data is provided in Table 2.

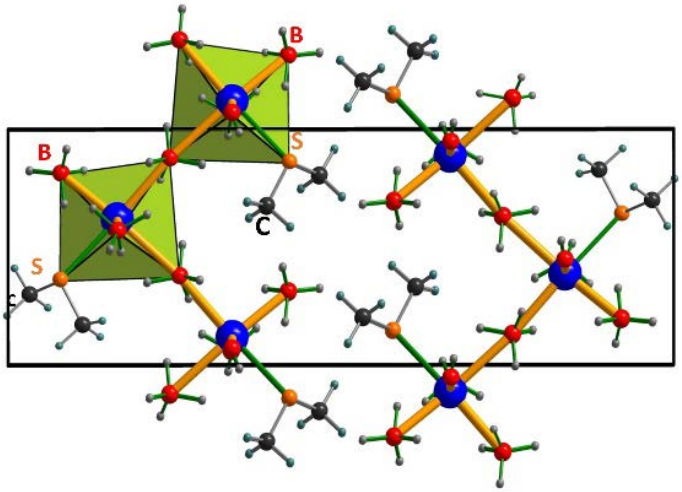

Figure 1 Crystal structure of $Pr(^{11}BD_4)_3S(CH_3)_2$ and $Nd(BH_4)_3S(CH_3)_2$.

3.2.2 Crystal structure of α-RE(BH$_4$)$_3$

The room temperature polymorphs of praseodymium(III) and neodymium(III) borohydrides, α-RE$(BH_4)_3$, RE = Pr, Nd, crystallize in space group $Pa\bar{3}$ and are isostructural to RT polymorphs of α-Y$(BH_4)_3$ and α-Gd$(BH_4)_3$.[20,36,38] The rare-earth atoms coordinate to six BH_4^- units with two different RE-B distances, i.e. Pr-B of 2.8535(1) and 2.8679(1) Å, and Nd-B of 2.8306(1) and 2.8449(1) Å, respectively, forming a distorted octahedral geometry. BH_4^- complexes are bridging the RE^{3+} centers with bidentate (η^2) coordination resulting in a 12-fold coordination of RE to hydrogen (Figure 2, middle).

3.2.3 Crystal structure of β-RE(BH$_4$)$_3$

Two different space groups of $Fm\bar{3}c$ and $Pm\bar{3}m$ have been reported for β-RE$(BH_4)_3$ as a high-temperature polymorph. The $Fm\bar{3}c$ structure has a fully ordered array of $[BH_4]^-$ groups, with 8 formula units in the unit cell, while the $Pm\bar{3}m$ structure has half the lattice parameter and the unit cell contains one formula unit.[20,37,38] The BH_4^- complexes randomly take either of the two possible orientations in the $Pm\bar{3}m$ structure. The X-ray diffraction patterns of

these two structural models are similar and cannot be distinguished. However, neutron powder diffraction of $Y(BH_4)_3$ has shown that the $Fm\bar{3}c$ structure is the correct space group.[37,38]

High temperature polymorphs, β–$RE(BH_4)_3$, RE = Pr, Nd ($Fm\bar{3}c$), are formed when α–$RE(BH_4)_3$ is heated under high hydrogen pressures. The β– polymorphs are isostructural to β-$RE(BH_4)_3$, RE = Ce, Sm, Ho, Y, Er, Tm, Yb, with straight RE-BH_4-RE coordination (η^2), which is isostructural to the ideal cubic ReO_3 structure (Figure 2, bottom). The RE atoms coordinate to six BH_4^- units with the same distance of Pr-B = 2.7859(2) Å (*T* = 190 °C) and Nd-B = 2.7847(3) Å (*T* = 269 °C), forming an ideal octahedral geometry in comparison to the distorted octahedron observed for the α-$RE(BH_4)_3$.[37] The β– polymorphs also have a bidentate (η^2) coordination of RE to BH_4^- forming a 12-fold coordination of RE to hydrogen. This structure contains large unoccupied voids at (¼, ¼, ¼) coordinate with a distance of ~3.35 Å from the center to the nearest hydrogen atom (Figure 2, bottom).[34]

3.2.4 Crystal structure of *r*-$RE(BH_4)_3$

A rhombohedral deformation of cubic β-$Pr(BH_4)_3$, denoted *r*-$RE(BH_4)_3$, that crystalizes in the trigonal crystal system with space group $R\bar{3}c$ (*Z* = 6) is also observed, which is isostructural to a high-pressure polymorph of rhenium trioxide, ReO_3.[54] *r*-$RE(BH_4)_3$ has been observed as the room temperature polymorph for RE = La, Ce. However, *r*-$Pr(BH_4)_3$ forms at *T* > 190 °C and the structure has been confirmed by Rietveld refinement of NPD data of *r*-$Pr(^{11}BD_4)_3$ (Figure **S11**). Six BH_4^- complexes are coordinated to each Pr^{3+} ion forming a regular octahedra, Pr-B distance of 2.8395(16) Å, similar to that observed in β-$Pr(BH_4)_3$.

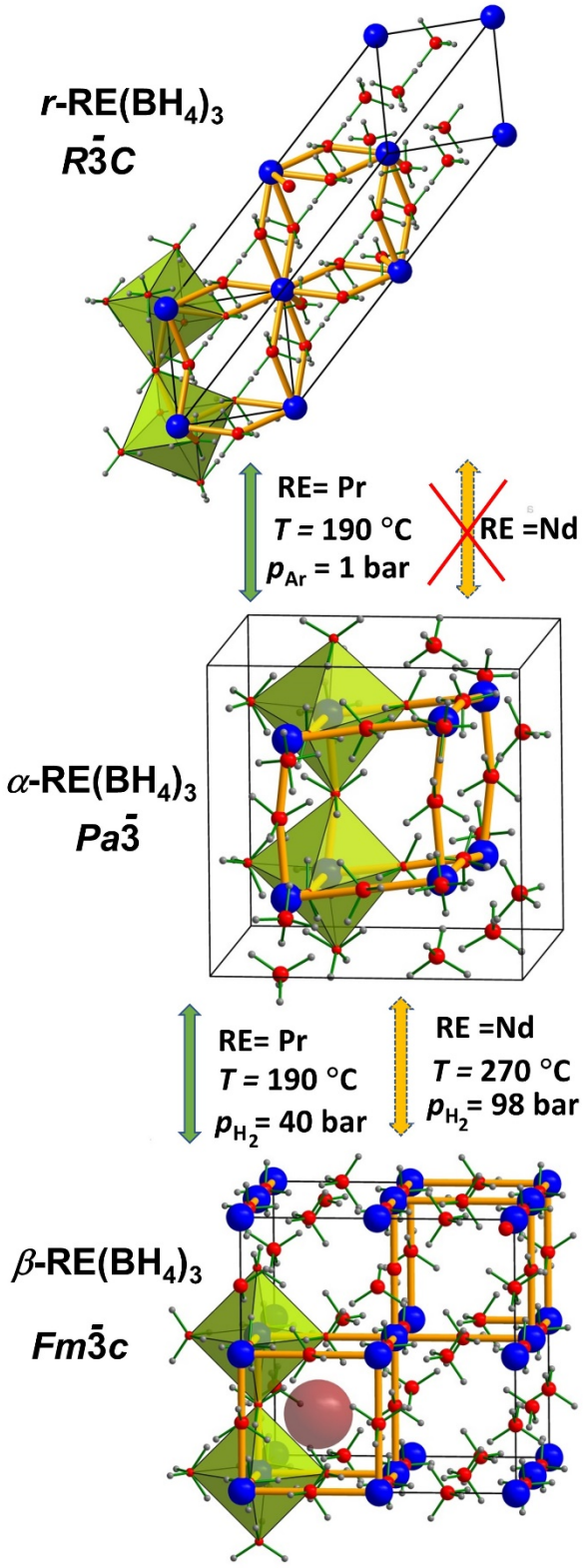

Figure 2 Crystal structures of (top) *r*-$Pr(BH_4)_3$, $\boldsymbol{R\bar{3}c}$, (middle) α-$RE(BH_4)_3$, $\boldsymbol{Pa\bar{3}}$, and (bottom) β-$RE(BH_4)_3$, $\boldsymbol{Fm\bar{3}c}$. One of the empty voids in the β-$Pr(BH_4)_3$ structure is shown with a (reddish/violet) sphere.

Table 2 Structural data extracted from Rietveld refinements of the XRPD and NPD data for $Pr(BH_4)_3S(CH_3)_2$, different polymorphs of $Pr(BH_4)$ and β''-$Nd(BH_4)_3$.

Sample	**$Pr(^{11}BD_4)_3S(CH_3)_2$**	**α-$Pr(BH_4)_3$**	**β''-$Pr(BH_4)_3$**	***r*-$Pr(^{11}BD_4)_3$**	**β''-$Nd(BH_4)_3$**
Crystal system	monoclinic	cubic	cubic	trigonal	cubic
Space group	$P2_1/c$	$Pa\bar{3}$	$Fm\bar{3}c$	$R\bar{3}c$	$Fm\bar{3}c$
***T* (°C)** ***p*(Ar, H_2)(bar)**	RT *p*(Ar) = 1	RT *p*(Ar) = 1	190 *p*(H_2) = 40	160 *p*(Ar) = 1	269 *p*(H_2) = 98
***a* (Å)**	5.6950(2)	11.2941(5)	11.1438(7)	7.373(6)	11.1386(1)
***b* (Å)**	22.9167(1)	-	-		-
***c* (Å)**	8.2400(4)	-	-	19.89(2)	-
***β* (°)**	100.68(0)	90	90	120	90
RE-B (Å) (1)	-	2.8607(1)	2.7859(2)	2.8395(16)	2.7847(3)
Z	4	8	8	6	8
***V* (Å^3)**	1056.78(60)	1440.64(11)	1383.88(15)	936.38(14)	1381.95(21)
***V*/*Z* (Å^3)**	264.2	180.1	172.98	156.1	172.7
ρ (g cm^{-3})	1.6318	1.7098	1.7801	2.1015	1.8146
ρv (H_2) **(kg H_2m^{-3})**	114.0427	111.5413	116.1161	257.1704	116.2783
ρm (H_2) (wt%)	7.3284	6.5226	6.5226	12.2370	6.4074
Radiation	X-ray	X-ray	X-ray	Neutron	X-ray

(1) Pr-B distance for α-$Pr(BH_4)_3$ is calculated based on the average of two Pr-B distances in the structure.

3.2.5 DFT optimisation of the $Pr(BH_4)_3$ polymorphs

Period plane wave DFT calculations of the three polymorphs were attempted in order to shed light on their properties. The structure of α-$Pr(BH_4)_3$, (the $Pa\bar{3}$ form), has been fully optimized with no constraints (128 atoms; for this large cell, Z = 8, a Monkhorst-Pack grid of 1×1×1 was selected). The calculations were performed adopting an antiferromagnetic structure, in which half of the Pr atoms have positive magnetization and half negative, with a total magnetization equal to zero. Calculations with different magnetization scheme failed to converge. By this approach, the optimized cell volume is larger than the experimental one by only 1.27 %, and final geometry and ions positions in the cell are very similar to the starting one. Similar calculations on the $Fm\bar{3}c$ and the $R\bar{3}c$ structures resulted in a significantly larger unit cell, +12.3% and +20.5%, respectively. The overestimation of the unit cell size is likely due to neglecting of phonon interactions, which become significant at higher temperatures required to convert $Pr(BH_4)_3$ to the $Fm\bar{3}c$ and $R\bar{3}c$ polymorphs. Therefore, a

simplified approach was adopted, which allows comparing the energy of the three different structures: only the atom positions within the unit cell were optimized with unit cell parameters fixed to the experimental values. By this method, the $Pa\bar{3}$ structure computed by DFT is the most stable, with the $Fm\bar{3}c$ and the $R\bar{3}c$ higher in energy by 4.3 and 6.4 kcal/mol, respectively, corresponding to decreasing stability of α–$Pr(BH_4)_3$ > β–$Pr(BH_4)_3$ > *r*–$Pr(BH_4)_3$. Moreover, DFT calculations of the *r*-$Pr(^{11}BD_4)_3$ structure obtained by NPD and with fixed unit cell parameters shows 7.4 kcal/mol higher energy than the $Pa\bar{3}$ structure. However, this relative energy order could be easily modified at higher temperatures, because the energy values of the three structures are close to each other.

3.3 *In Situ* Synchrotron Radiation X-ray Powder Diffraction

3.3.1 Investigation of $Pr(BH_4)_3$ polymorphism as a function of *p,T*

The thermal properties of $Pr(^{11}BD_4)_3S(CH_3)_2$ in *p*(Ar) = 1 bar are investigated by *in-situ* SR-XRPD, see Figure 3. Only the Bragg reflections of the solvate compound are observed at RT. At *T* > 130 °C, $Pr(^{11}BD_4)_3S(CH_3)_2$ decompose with release of $S(CH_3)_2$, and formation of two different polymorphs of praseodymium(III) borohydride, α- and β-$Pr(^{11}BD_4)_3$, 66.8(3) and 33.2(3) wt%, respectively (Figure S1). Further heating of the sample leads to decreasing degree of long range order of the β polymorphs (i.e. decreasing diffracted intensity of β) and an apparent increasing amount of α-$Pr(^{11}BD_4)_3$. This occur because the sample composition is normalized to 1 (notice that the diffracted intensity of α appear constant in the temperature range ~150 to ~180 °C). The Bragg reflections of β-$Pr(^{11}BD_4)_3$ are abruptly shifted to higher 2θ angles at ~176 °C with a similar abrupt increase of the diffracted intensity, revealing a contraction of the unit cell and the formation of a new polymorph denoted β'-$Pr(BH_4)_3$ ($Fm\bar{3}c$) (not shown in figure 3b because of the overlap of the Bragg reflections of α and β' phases at 2θ = 7.2 and 10.2), At the same time, the fraction of this polymorph, β'-, increases

and reaches a maximum of 33.5(9) wt% at 185 °C (Figure 3b). At T = 190 °C, α-Pr($^{11}BD_4$)$_3$ disappears, and *r*-Pr($^{11}BD_4$)$_3$ with the smallest V/Z forms as the major polymorph, 89(1) wt%. Simultaneously, the unit cell volume of β'-Pr($^{11}BD_4$)$_3$ shrinks for the second time to V/Z ~ 170.9 Å^3, forming a polymorph denoted β''-Pr($^{11}BD_4$)$_3$ (displayed by arrows in Figure 3a). The structural mechanism for formation of the four polymorphs of praseodymium (III) borohydride is discussed in section 3.5.

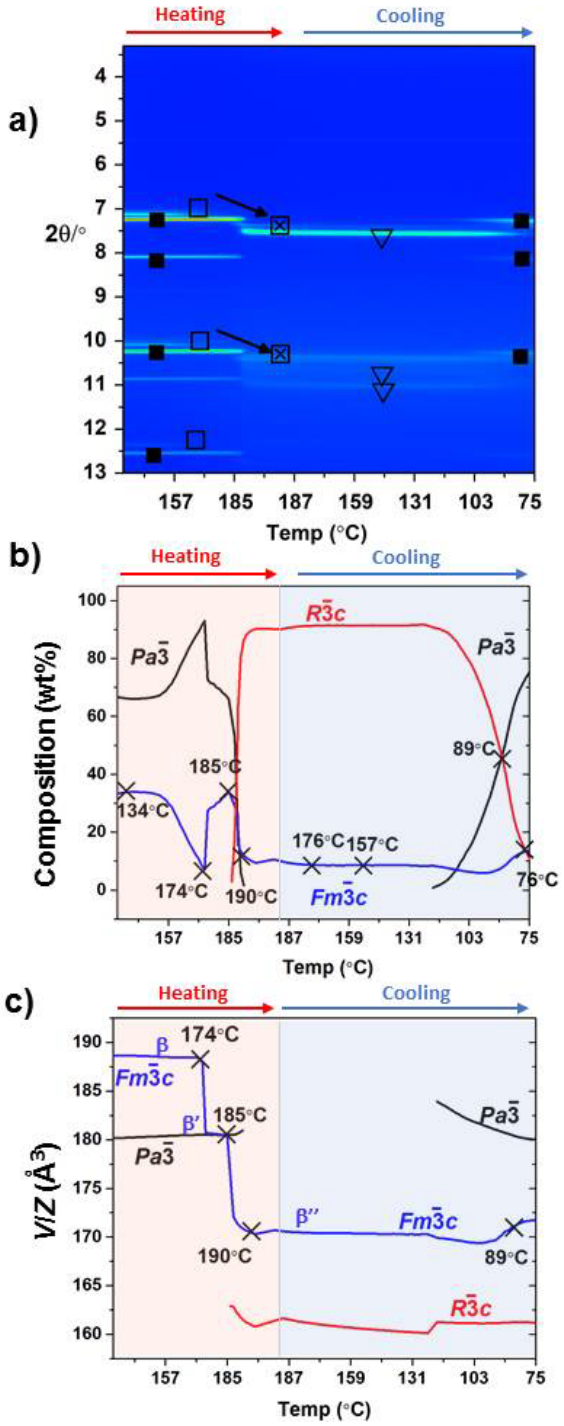

Figure 3 (a) *In-situ* SR-XRPD data of $Pr(^{11}BD_4)_3S(CH_3)_2$ compound under p(Ar) = 1 bar. $\Delta T/\Delta t$ = 5 °C/min (λ = 0.7129 Å). Symbols: ● $Pr(^{11}BD_4)_3S(CH_3)_2$; ■ α-$Pr(^{11}BD_4)_3$ $Pa\bar{3}$; □ β-$Pr(^{11}BD_4)_3$ $Fm\bar{3}c$; ⊠ β''-$Pr(^{11}BD_4)_3$ $Fm\bar{3}c$ and ▽ for r-$Pr(^{11}BD_4)_3$ $R\bar{3}c$; (b) Sample composition and (c) V/Z of each polymorph extracted by Rietveld refinement of the SR-XRPD data.

Upon cooling, the polymorphs *r*– and β**’’**-Pr($^{11}BD_4$)$_3$ are stable to 119 °C where α-Pr($^{11}BD_4$)$_3$ starts to form on the expense of *r*-Pr($^{11}BD_4$)$_3$. Further cooling of the sample fully transforms the *r*-Pr($^{11}BD_4$)$_3$ to α-Pr($^{11}BD_4$)$_3$ and the sample composition at 59 °C is, α-Pr($^{11}BD_4$)$_3$ 83(1) wt% and β**’’**-Pr($^{11}BD_4$)$_3$ 17.5(7) wt%. The *in-situ* SR-XRPD data of Pr(BH_4)$_3$ heated under *p*(Ar) = 1 bar (see Figure **S2**) is similar to that presented in Figure 3 of Pr($^{11}BD_4$)$_3$S(CH_3)$_2$.

A second series of *in-situ* XRPD experiments were performed in hydrogen atmosphere, *p*(H_2) = 40 bar, in order to investigate the possible effect of gas and partial pressure on the structural evolution, and the data are presented in Figures 4a and S3. *In-situ* SR-XRPD of Pr(BH_4)$_3$ at RT, reveal diffractions from the polymorphs α- (94.7(3) wt%) and β-Pr(BH_4)$_3$ (5.3(2) wt%), see Figure 4b. Prior to this experiment Pr(BH_4)$_3$ has been annealed at 180 °C and the observed sample composition is similar to the one observed in the previous experiment at 174 °C using Pr($^{11}BD_4$)$_3$S(CH_3)$_2$ (Figure 3b). An abrupt displacement of the β-Pr(BH_4)$_3$ Bragg reflections towards lower 2θ angles is also observed in this case, at 174 °C, and is assigned to the formation of β**’**-Pr(BH_4)$_3$. Moreover, the unit cell volume of β**’**-Pr(BH_4)$_3$ shrinks for the second time upon formation of β**’’**-Pr(BH_4)$_3$. However, noteworthy, β**’’**-Pr(BH_4)$_3$, 66.6(8) wt%, is now the main component in the sample at 190 °C. The stabilization of the cubic and porous β**’’**-Pr(BH_4)$_3$ in larger amounts here contrasts the formation of *r*-Pr(BH_4)$_3$, 89(1) wt%, at 190 °C, in the previous measurement (Figure 3b). At *T* = 190 °C, the Bragg reflections of α-Pr(BH_4)$_3$ disappear and *r*-Pr(BH_4)$_3$ forms in smaller amounts. This clearly shows the strong influence of gas and partial pressures for the polymorphism of Pr(BH_4)$_3$. Upon cooling, β**’’**-Pr(BH_4)$_3$ remains as the major polymorph to 157 °C where transformation to α-Pr(BH_4)$_3$ starts.

The extracted unit cell volumes (*V*/*Z*) as a function of temperature (Figure 4c) show that the β''-$Pr(BH_4)_3$ structure is ~10 $Å^3$ more expanded as compared to *r*-$Pr(BH_4)_3$ upon cooling in the temperature range 190 to ~100 °C, for both experiments (Figure 3c and 4c).

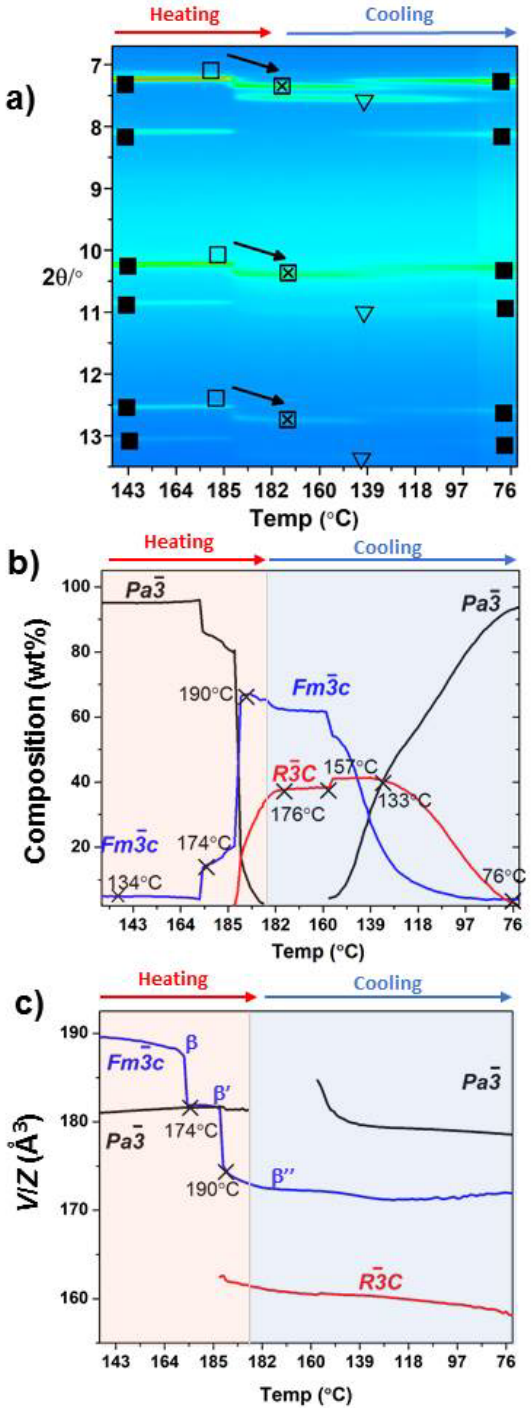

Figure 4 (a) *In-situ* SR-XRPD data of $Pr(BH_4)_3$ compound under $p(H_2)$ = 40 bar. $\Delta T/\Delta t$ = 5 °C/min (λ = 0.7129 Å), symbols: ■ α-$Pr(BH_4)_3$ $Pa\bar{3}$; □ β-$Pr(BH_4)_3$ $Fm\bar{3}c$; ⊠ β''-

$Pr(BH_4)_3$ $Fm\bar{3}c$ and ▽ for *r*-$Pr(BH_4)_3$ $R\bar{3}c$; (b) Sample composition and (c) *V*/*Z* of each polymorph extracted by Rietveld refinement of SR-XRPD data.

3.3.2 Investigation of $Nd(BH_4)_3$ polymorphism as a function of *p,T*

The neodymium borohydride solvate, $Nd(BD_4)_3S(CH_3)_2$ (**s4**), was also investigated by *in-situ* SR-XRPD under *p*(Ar) = 1 bar, see Figure S3, and Bragg reflections of this compound are observed in the temperature range RT to 165 °C. $Nd(BD_4)_3S(CH_3)_2$ decomposes with release of $S(CH_3)_2$ and formation of α-$Nd(BD_4)_3$, at *T* > 165 °C. However, no polymorphic transitions are observed for $Nd(BH_4)_3$ by further heating, and the sample starts to decompose at *T* ~ 213 °C.

In-situ SR-XRPD of $Nd(BH_4)_3$ under $p(H_2)$ = 98 bar has also been measured, see Figure S4. At RT, the sample contains α-$Nd(BH_4)_3$, 93(1) wt%, and β-$Nd(BH_4)_3$, 6.8(5) wt%. Similar to the $Pr(BH_4)_3$, when the sample is heated in hydrogen pressure, stepwise polymorphic transition is observed β- → β**'**- → β**''**-$Nd(BH_4)_3$, i.e. another rare example of negative thermal expansion. This sample fully transforms to β''-$Nd(BH_4)_3$ at 270 °C, which is in contrast to formation of only 66.6(8) wt% of β''-$Pr(BH_4)_3$ in the previous experiment. These polymorphic transitions are reversible, and Bragg reflections of α-$Nd(BH_4)_3$ starts to appear upon cooling at *T* ~ 230 °C. The observation of polymorphic transition at higher temperatures for $Nd(BH_4)_3$ (*T* = 270 °C) and the suppression of decomposition is clearly due to the elevated hydrogen pressure used in this experiment.

3.4 Atomic distances in praseodymium(III) borohydride as a function of *p,T*

The Pr-B distances and weight fractions of praseodymium(III) borohydride polymorphs obtained from Rietveld refinements of *in-situ* SR-XRPD data at *p*(Ar) = 1 bar and selected temperatures are shown in Figure 5. The α-$Pr(^{11}BD_4)_3$ polymorph (67.8(3) wt%) has Pr-B distance of 2.8611(1) Å, at *T* = 134 °C. The major component at 190 °C, *r*-$Pr(^{11}BD_4)_3$ (95(2)

wt%) has longer Pr-B distance 2.9236(4) Å due to transverse rotation of $Pr(BD_4)_6$ octahedra. In this process, the B atom in the middle of the Pr−B−Pr linkage is displaced transversely, the Pr-B distance is increased, and the two Pr atoms are pulled together, inducing a contraction in the unit cell volume. Upon cooling to 76 °C, α-$Pr(^{11}BD_4)_3$ (73(1) wt%) forms with shorter Pr-B distance of 2.8606(1) Å as compared to the *r*-polymorph.

Figure 5 Pr-B distances of each $Pr(BH_4)_3$ polymorph at different temperatures under *p*(Ar) = 1 bar obtained by Rietveld refinement of XRPD data (Figure 3a). The weight percent of the polymorphs at each temperature is written in the figures. Dash line connects the polymorphs with the highest amount (wt%) at each temperature. Symbols: ■ α-$Pr(BH_4)_3$ $\boldsymbol{Pa\bar{3}}$; □ β-$Pr(BH_4)_3$ $\boldsymbol{Fm\bar{3}c}$; ⊠ β''-$Pr(BH_4)_3$ $\boldsymbol{Fm\bar{3}c}$ and ▽ for *r*-$Pr(BH_4)_3$ $\boldsymbol{R\bar{3}c}$.

The Pr-B distances of the different polymorphs of $Pr(BH_4)_3$ during heat treatment under *p*(H_2) = 40 bar are shown in Figure 6. At 134 °C, α-$Pr(BH_4)_3$, 88.7(5) wt%, is the dominant polymorph with Pr-B distances of 2.8654(1) Å. Increasing the temperature facilitate formation of the β-polymorphs with distinct Pr-B distances of 2.8726(1), 2.8321(2) and 2.7859(2) Å for β-, β'- and β''- measured at 134, 185 and 190 °C, respectively.

These results reveal that the type of gas (Ar or H_2) and partial pressures influence the Pr-B bond lengths. When experiments are performed in argon complete rotation of $Pr(BH_4)_6$ octahedra occurs and *r*-$Pr(BH_4)_3$ with longer Pr-B distance forms. However, in hydrogen, the porous β polymorphs stabilize with straight Pr-BH_4-Pr coordination and shorter Pr-B distances.

Figure 6 Pr-B distances of each $Pr(BH_4)_3$ polymorph at different temperatures under $p(H_2)$ = 40 bar. The sample composition (wt%) at each temperature is given in the figure with a dash line connecting the polymorphs in highest amount. Symbols: ■ α-$Pr(BH_4)_3$ $\boldsymbol{Pa\bar{3}}$; □ β-$Pr(BH_4)_3$ $\boldsymbol{Fm\bar{3}c}$; ⊠ β''-$Pr(BH_4)_3$ $\boldsymbol{Fm\bar{3}c}$ and ▽ for *r*-$Pr(BH_4)_3$ $\boldsymbol{R\bar{3}c}$.

3.5 Mechanism for transformation of praseodymium(III) borohydride polymorphs

The three polymorphs α-, β- and *r*-$Pr(BH_4)_3$, have the rhenium(VI) trioxide, ReO_3, structure types. In an ideal cubic ReO_3 structure, the Re atoms occupy the corners of the cube and coordinate to six oxygen atoms placed on the centers of the edges. This is also the case for the cubic β-$Pr(BH_4)_3$ with Pr-B-Pr bond angles of 180°. This structure type is closely related to the perovskite structure, *i.e.* $SrTiO_3$, but without the Sr atoms located on the center of the cube leaving an empty void in this position (see Figure 2).[55]

A wide variety of crystal structures can be derived by coupled rotation of octahedra, i.e. $[RE(BH_4)_6]$, without breaking or forming chemical bonds, such as α- and *r*-$Pr(BH_4)_3$, which crystalize in distorted ReO_3 structures. At RT, α-$Pr(BH_4)_3$ is stable, which unfolds to the ideal ReO_3 structure, β-$Pr(BH_4)_3$, upon heating, but this polymorph is unstable and transforms to *r*-$Pr(BH_4)_3$ (Figures 7). The transformation of β to *r*- polymorph is assigned to the large voids in the β-polymorph that allow bending of the Pr-B-Pr linkage, which increases the Pr-B bond distance, decrease the Pr-Pr distance by rotation of $Pr(BH_4)_6$ octahedra and consequently contract the unit cell volume. The transformation of β- to *r*-$Pr(BH_4)_3$ occurs via two other polymorphs, β'- and β''-$Pr(BH_4)_3$ as further discussed below. The polymorphs β- and *r*-$Pr(BH_4)_3$ are only stable at elevated temperatures and transform back to α-$Pr(BH_4)_3$ at RT, possibly due to H-H repulsion.

The relationship between hexagonal(*r*) and cubic(β) unit cell parameters in an ideal cubic crystal system is $a(r) = \frac{a(\beta) \times \sqrt{2}}{2}$ and $c(r) = a(\beta) \times \sqrt{3}$. The values determined from the Rietveld refinement of *r*- and β''-$Pr(BH_4)_3$ at 190 °C are $a(r)$ = 7.4831(12), $c(r)$ = 19.995(5) and $a(\beta'')$ = 11.1438(7) Å, respectively. Therefore, the calculation of the non-deformed hexagonal unit cell from cubic cell is $a(r) = \frac{11.1438 \times \sqrt{2}}{2} =$ 7.8798 Å and $c(r) = 11.1314 \times \sqrt{3} = 19.3016$ Å. This shows that the rhombohedral structure is compressed along $a(r)$ and expanded along $c(r)$. The same deformation has been observed for $Ce(BH_4)_3$ and $La(BH_4)_3$ polymorphs.[34]

The cubic to rhombohedral β- to *r*-$Pr(BH_4)_3$ transformation deserve more attention. This transformation clearly occurs via two intermediate polymorphs, β'- and β''-$Pr(BH_4)_3$, with distinct unit cell differences as illustrated in Figure 3c and 4c. The extracted unit cell volumes (V/Z) as a function of temperature reveal gradual decrease of ~8-10 $Å^3$ per transformation in

the series: β- → β'- → β''- → *r*-$Pr(BH_4)_3$. The *V*/*Z* values suggest that ~1/3 and ~2/3 of the original cubic structure is contracted to the rhombohedral structure type in β'- and β''-$Pr(BH_4)_3$ ($p(H_2)$ = 40 bar). This suggest static disorder created by rotation of $[Pr(BH_4)_6]$ octahedra, which reduce the Pr-Pr distance and result in decrease in unit cell volume. A dynamic effect, such as transverse vibration of BH_4 complexes normal to the Pr-Pr axis or rotation around this axis may occur. However, that is expected to provide a gradual change of unit cell volume as a function of temperature, in contrast to the stepwise changes clearly shown in Figure 3c and 4c.

A similar behavior has also been observed for ScF_3 with the identical cubic ReO_3 structure type responsible for negative thermal expansion (NTE) and zero thermal expansion (ZTE) of $(Sc_{0.85}Ga_{0.05}Fe_{0.1})F_3$.[56,57] However, unlike $Pr(BH_4)_3$, continuous contraction of unit cell volume is observed for ScF_3. For these fluorides, the collapse in the unit cell volume upon heating is attributed to the partial formation of a rhombohedral structure in a cubic-like form rather than a rhombohedral unit cell. In this case, the long-range structure remains cubic, but the local structure is distorted in a similar way as in the rhombohedral polymorph, which makes it very challenging to identify by XRPD. This occurs due to transverse vibration of fluoride anions, i.e. a dynamic effect.[56]

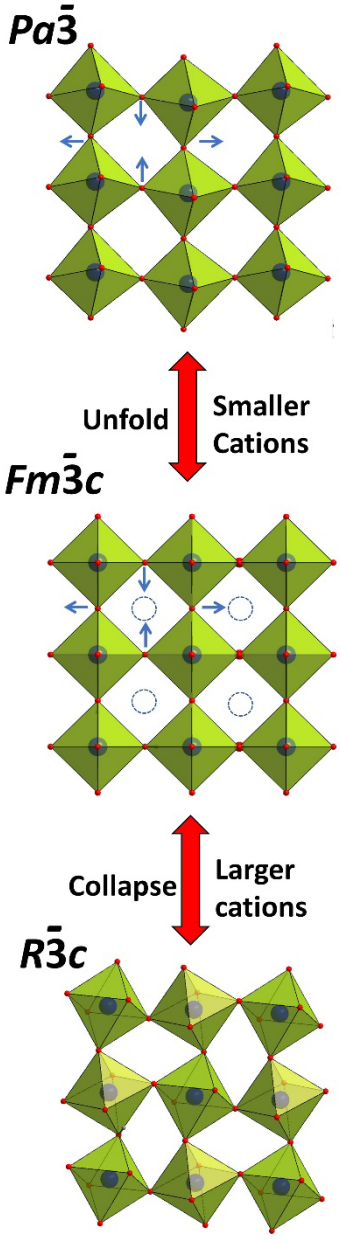

Figure 7 The REB_6 polyhedra in space groups symmetries $\boldsymbol{Pa\bar{3}}$, $\boldsymbol{Fm\bar{3}c}$ and $\boldsymbol{R\bar{3}c}$. The empty voids in the $\boldsymbol{Fm\bar{3}c}$ structure are presented by (blue dashed) empty circles.

We observe that ~95 wt% of $Pr(BH_4)_3$ transforms completely to the rhombohedral polymorph upon heating in argon, p(Ar) = 1 bar, *i.e*. the structure becomes rhombohedral both locally and over long range. However, a minor amount keeps the cubic long range order and shows a stepwise decrease of unit cell volume, i.e. β'- (20 wt% at 185 °C) and β''-$Pr(BH_4)_3$ (5 wt% at 190 °C). Hydrogen gas, $p(H_2)$ = 40 bar, clearly facilitate the stepwise polymorphic transitions

β- → β'- → β''- → α-$Pr(BH_4)_3$ upon heating/cooling of ~65 wt% of the sample. A similar trend is observed for neodymium(III) borohydride with no observation of β-polymorphs in argon but increasing amount in hydrogen, i.e. 7.9(6), 17(1) and 100 wt% of β- → β'- → β''-$Nd(BH_4)_3$, at 134, 173, 190 and 270 °C.

3.6 Comparison of the crystal structures of the different $RE(BH_4)_3$ compounds

The series of rare earth borohydrides show significant structural changes as a function of small changes in the cation ionic radii. The largest rare-earth metal borohydrides, La and Ce, crystalize as the polymorph *r*-$RE(BH_4)_3$ at RT and have smaller unit cell volumes and higher densities compared to the cubic structure type, α-$RE(BH_4)_3$. The smaller RE elements crystallize in cubic structures, e.g. as α-$Pr(BH_4)_3$. This work highlights praseodymium as a 'boarder line' RE element, which exist in five different polymorphs α-, β-, β'-, β''-, and *r*-$Pr(BH_4)_3$. This trend, presented in Figure 8, suggests that the crystal structures of the rare-earth metal borohydrides are dependent on the size of the cation.

Previous experiments have shown that β-$Ce(BH_4)_3$ is only formed when $Ce(BH_4)_3S(CH_3)_2$ is heated in a closed capillary, and that annealing under dynamic vacuum forms the *r*-polymorph. Our experimental work reveal that formation of β-$Pr(BH_4)_3$ and two intermediate polymorphs, β'- and β''-$Pr(BH_4)_3$ can be facilitated by $p(H_2)$ = 40 bar and T = 175 and 190 °C, respectively. Thus, presence of gasses clearly facilitate stabilization of the β-polymorphs.

The radius of neodymium ion is slightly smaller as compared to praseodymium, $r(Nd^{3+})$ = 1.123 and $r(Pr^{3+})$ = 1.130 Å,[58] and a different polymorphism of $Nd(BH_4)_3$ is discovered in this study. No polymorphic changes are observed during heating of *α*-$Nd(BH_4)_3$ in argon, however, β''-$Nd(BH_4)_3$ forms when heated in hydrogen ($p(H_2)$ = 98 bar) and at T = 270 °C.

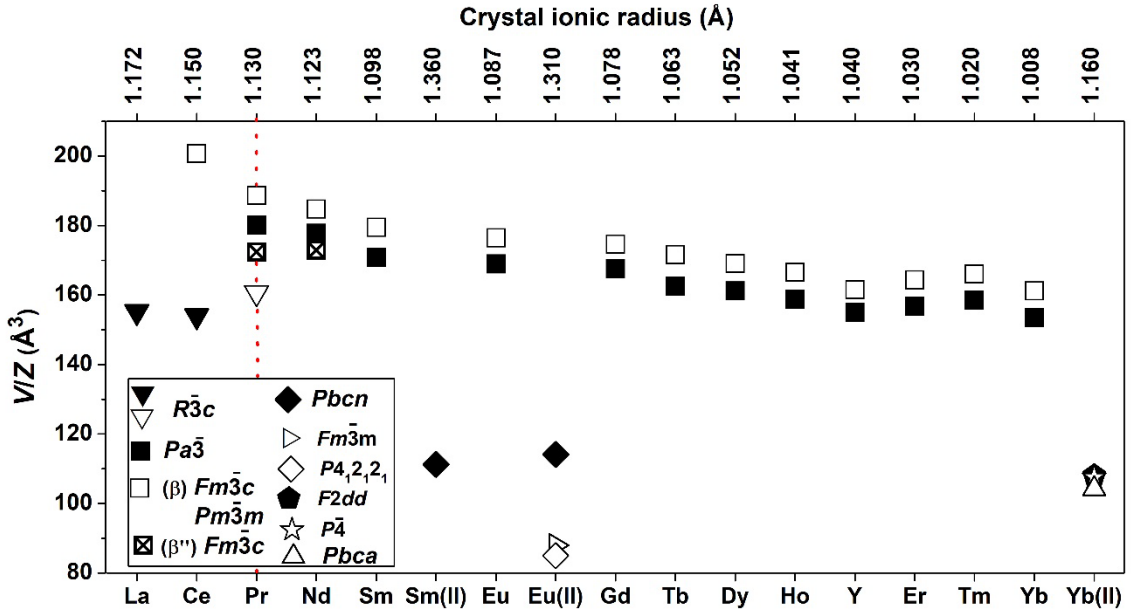

Figure 8 Unit cell volumes (*V*) divided by the number of formula units (*Z*) of the reported rare-earth borohydrides. Two values are shown for the *V*/*Z* of β-RE$(BH_4)_3$, RE = Pr, Nd. α and β polymorphs of Pr$(BH_4)_3$ and Nd$(BH_4)_3$ polymorphs are recorded at RT while β'' polymorphs are recorded at 190 and 269 °C respectively.[19–21,23,24,34,35,39,59,60] The ionic radii are taken from reference.[58] Polymorphs stable at RT are shown with a filled symbol (■). Space groups of $Fm\bar{3}c$ and $Pm\bar{3}m$ are presented by one symbol (□) because of the similarity of their structures.

3.7 Thermal analysis

Thermal analysis, TGA-DSC-MS, of Pr$(BH_4)_3$ (**s3**), Figure 9, reveal a total release of hydrogen of 4.8 wt%, which is lower than the calculated hydrogen content of 5.97 wt% according to the reaction scheme:

$2Pr(BH_4)_3 \rightarrow PrB_6 + PrH_2 + 11H_2$

Two endothermic peaks are observed in the DSC data, one at 204 °C is assigned to the first order polymorphic transition of α-Pr$(BH_4)_3$ to *r*-Pr$(BH_4)_3$ and the second at 247 °C to the decomposition of the sample. In order to investigate the reversibility of the polymorphic transition, a second experiment was conducted by heating the sample to 220 °C and cooling back to RT. Figure 9b shows that the sample releases ~0.5 wt% of hydrogen during the α to *r*-polymorphic transition temperature. Upon cooling the sample to RT, an exothermic peak is

observed in the DSC curve at 125 °C. This event is attributed to the polymorphic transition of *r*- to α-$Pr(BH_4)_3$ and is in good agreement with the reformation of α-$Pr(BH_4)_3$ at 119 °C observed by *in-situ* SR-XRPD experiment.

Thermal analysis, TGA-DSC-MS, of $Nd(BH_4)_3$ is shown in Figure S14, and reveal one endothermic peak in the DSC data, at T ~ 250 °C, assigned to decomposition. A release of 5.5 wt% of hydrogen is observed in the temperature range 200 to 400 °C, which is slightly lower than the calculated hydrogen content, 5.87 wt% based on the reaction:

$2Nd(BH_4)_3 \rightarrow NdB_6 + NdH_2 + 11H_2$.

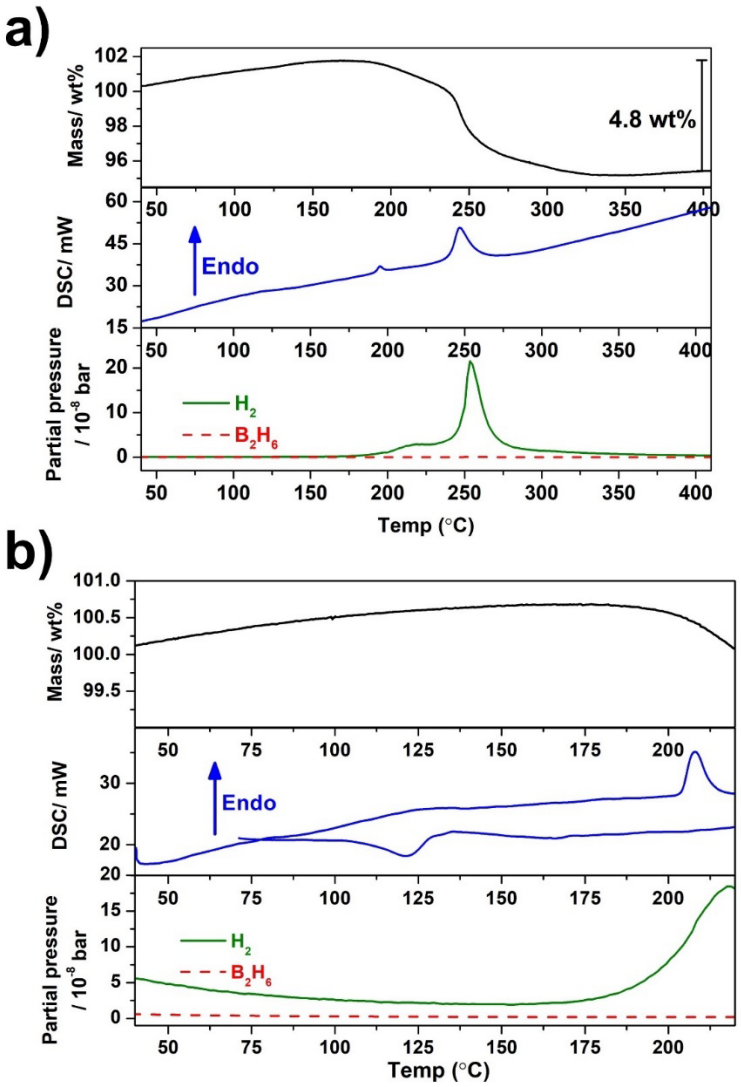

Figure 9 (a) TGA-DSC-MS data for $Pr(BH_4)_3$ (**s3**) heated from RT to 400 °C (in argon flow). Upper part: The TGA curve in black. Middle: DSC curve in blue and the corresponding MS

signals in lower part for hydrogen and diborane presented by green and red curves, respectively. (b) TGA-DSC-MS data for $Pr(BH_4)_3$ (**s3**) heated from RT to 220 °C and cooled back to RT ($\Delta T/\Delta t$ = 5 °C/min).

4. Conclusion

In this study, the $Pr(^{11}BD_4)_3S(CH_3)_2$ and four new polymorphs *r*- and β-, β'- and β''-$Pr(BH_4)_3$ are presented, which highlights $Pr(BH_4)_3$ as a 'boarder-line' rare earth metal borohydride with unique crystal chemistry. At RT, α-$Pr(BH_4)_3$ ($Pa\bar{3}$) is formed, and at T = 190 °C the structure transforms to the more dense polymorph *r*-$Pr(BH_4)_3$ ($R\bar{3}c$). The cubic (β-) to rhombohedral, *r*-$Pr(BH_4)_3$ transformation occur via two intermediate polymorphs, β'- and β''-$Pr(BH_4)_3$, with distinct decrease of unit cell volumes, and is a rare example of stepwise negative thermal expansion. This suggest static disorder created by rotation of $[Pr(BH_4)_6]$ octahedra, which reduce the Pr-Pr distance and result in decrease in unit cell volume. A similar, but continuous, change of volume is observed for the isostructural ScF_3 with the same cubic ReO_3 structure type responsible for negative thermal expansion (NTE) due to a dynamic structural effect.

We observe that ~95 wt% of $Pr(BH_4)_3$ transforms completely to the rhombohedral polymorph upon heating in argon (p(Ar) = 1 bar), *i.e.* the structure becomes rhombohedral both locally and over long range. However, a minor amount, ~5 wt%, of $Pr(BH_4)_3$ keeps the cubic long range order and shows a stepwise decrease of unit cell volume. Hydrogen gas ($p(H_2)$ = 40 bar) clearly facilitate the stepwise polymorphic transitions α-$Pr(BH_4)_3$ → β- → β'- → β''- upon heating/cooling of ~65 wt% of the sample. These results reveal that the type of gas (Ar or H_2) and partial pressures have little influence on the characteristic bond lengths observed in the five polymorphs, which contrasts the strongly influence on the stability of the different polymorphs and the sample composition.

Neodymium borohydride, $Nd(BH_4)_3$, is also synthesized and the polymorphic transitions are compared to $Pr(BH_4)_3$. The smaller voids in $Nd(BH_4)_3$ are not large enough to allow the rotation of $Nd(BH_4)_6$ octahedra and formation of a rhombohedral polymorphs. However, the stepwise polymorphic transitions β- → β'- → β'' is also observed for this compound in the presence of hydrogen gas ($p(H_2)$ = 98 bar) and the sample completely transforms to β''-$Nd(BH_4)_3$ at T = 269 °C.

Acknowledgements

The research leading to these results has received funding from the People Program (Marie Curie Actions) of the European Union's Seventh Framework Program FP7/2007-2013/ under REA grants agreement no. 607040 (Marie Curie ITN ECOSTORE). Furthermore, the work was supported by the Danish National Research Foundation, Center for Materials Crystallography (DNRF93), the Danish Research Council for Nature and Universe (Danscatt) and Danish council for independent research (HyNanoBorN), DFF – 4181-00462. NordForsk and The Nordic Neutron Science Program is acknowledged for funding of FunHy (Project no. 81942). We are grateful to the Carlsberg Foundation. The accesses to the SNBL beamline at the ESRF Synchrotron, P02 beamline at Petra (III) synchrotrons and SINQ at Paul Scherrer institute are gratefully acknowledged.

References

1 L. Schlapbach and A. Züttel, Hydrogen-storage materials for mobile applications., *Nature*, 2001, **414**, 353–358.

2 R. Mohtadi and S. Orimo, The renaissance of hydrides as energy materials, *Nat. Rev.*

Mater., 2016, **2**, 16091.

3 T. He, P. Pachfule, H. Wu, Q. Xu and P. Chen, Hydrogen carriers, *Nat. Rev. Mater.*, 2016, **1**, 16059.

4 L. H. Jepsen, M. B. Ley, Y.-S. Lee, Y. W. Cho, M. Dornheim, J. O. Jensen, Y. Filinchuk, J. E. Jørgensen, F. Besenbacher and T. R. Jensen, Boron–nitrogen based hydrides and reactive composites for hydrogen storage, *Mater. Today*, 2014, **17**, 129–135.

5 M. B. Ley, L. H. Jepsen, Y.-S. Lee, Y. W. Cho, J. M. Bellosta von Colbe, M. Dornheim, M. Rokni, J. O. Jensen, M. Sloth, Y. Filinchuk, J. E. Jørgensen, F. Besenbacher and T. R. Jensen, Complex hydrides for hydrogen storage – new perspectives, *Mater. Today*, 2014, **17**, 122–128.

6 S. Orimo, Y. Nakamori, J. R. Eliseo, A. Zu and C. M. Jensen, Complex Hydrides for Hydrogen Storage, *Chem. Rev.*, 2007, **107**, 4111–4132.

7 M. Paskevicius, L. H. Jepsen, P. Schouwink, R. Ĉerný, D. B. Ravnsbæk, Y. Filinchuk, M. Dornheim, F. Besenbacher and T. R. Jensen, Metal Borohydrides and derivatives - synthesis, structure and properties, *Chem. Soc. Rev*, 2017, **46**, 1565–1634.

8 Y. Nakamori, K. Miwa, A. Ninomiya, H. Li, N. Ohba, S. Towata, A. Züttel and S. Orimo, Correlation between thermodynamical stabilities of metal borohydrides and cation electronegativites: First-principles calculations and experiments, *Phys. Rev. B*, 2006, **74**, 45126.

9 M. Heere, S. P. GharibDoust, M. Brighi, C. Frommen, T. R. Jensen and B. C. Hauback, Hydrogen Sorption in Erbium Borohydride Composite Mixtures with LiBH4 and/or LiH, *Inorganics*, 2017, **5**, 31.

10 M. Heere, S. P. GharibDoust, M. H. Sørby, C. Frommen, T. R. Jensen and B. C. Hauback, In situ investigations of bimetallic potassium erbium borohydride, *Int. J.*

Hydrogen Energy, 2017, **42**, 22468–22474.

11 C. Frommen, M. Heere, M. D. Riktor, M. H. Sørby and B. C. Hauback, Hydrogen storage properties of rare earth (RE) borohydrides (RE=La, Er) in composite mixtures with LiBH4 and LiH, *J. Alloys Compd.*, 2015, **645**, S155–S159.

12 S. P. GharibDoust, D. B. Ravnsbæk, R. Černý and T. R. Jensen, Synthesis, structure and properties of bimetallic sodium rare-earth (RE) borohydrides, $NaRE(BH_4)_4$, RE = Ce, Pr, Er or Gd, *Dalt. Trans.*, 2017, **46**, 13421–13431.

13 S. P. GharibDoust, M. Heere, M. H. Sørby, M. B. Ley, D. B. Ravnsbæk, B. C. Hauback, R. Černý and T. R. Jensen, Synthesis, structure and properties of new bimetallic sodium and potassium lanthanum borohydrides, *Dalt. Trans.*, 2016, **45**, 19002–19011.

14 C. Frommen, M. H. Sørby, M. Heere, T. D. Humphries, J. E. Olsen and B. C. Hauback, Rare Earth Borohydrides—Crystal Structures and Thermal Properties, *Energies*, 2017, **10**, 2115.

15 S. Marks, J. G. Heck, M. H. Habicht, P. On, C. Feldmann and P. W. Roesky, $[Ln(BH_4)_2(THF)_2]$ (Ln = Eu, Yb) Highly Luminescent Material. Synthesis, Properties, Reactivity, and NMR Studies, *J. Am. Chem. Soc.*, 2012, **2**, 16983–16986.

16 F. Bonnet, A. R. Cowley, P. Mountford, M. Road and O. Ox, Lanthanide Borohydride Complexes Supported by Diaminobis (phenoxide) Ligands for the Polymerization of E-Caprolactone and L - and rac-Lactide, *Inorg. Chem.*, 2005, **44**, 9046–9055.

17 F. Bonnet, M. Visseaux, A. Pereira and D. Barbier-Baudry, Highly trans-stereospecific isoprene polymerization by neodymium borohydrido catalysts, *Macromolecules*, 2005, **38**, 3162–3169.

18 S. M. Guillaume, M. Schappacher and A. Soum, Polymerization of ε-Caprolactone initiated by $Nd(BH_4)_3(THF)_3$: Synthesis of hydroxytelechelic poly(ε-caprolactone),

Macromolecules, 2003, **36**, 54–60.

19 M. Heere, S. H. Payandeh, C. Frommen, T. D. Humphries, M. B. Ley, M. H. Sørby, T. R. Jensen and B. C. Hauback, The influence of LiH on the rehydrogenation behavior of halide free rare earth (RE) borohydrides (RE = Pr, Er)., *Phys. Chem. Chem. Phys.*, 2016, **18**, 24387–24395.

20 D. B. Ravnsbaek, Y. Filinchuk, R. Cerný, M. B. Ley, D. Haase, H. J. Jakobsen, J. Skibsted and T. R. Jensen, Thermal polymorphism and decomposition of $Y(BH_4)_3$, *Inorg. Chem.*, 2010, **49**, 3801–3809.

21 T. D. Humphries, M. B. Ley, C. Frommen, K. T. Munroe, T. R. Jensen and B. C. Hauback, Crystal structure and in situ decomposition of $Eu(BH_4)_2$ and $Sm(BH_4)_2$, *J. Mater. Chem. A*, 2015, **3**, 691–698.

22 K. Park, H.-S. Lee, A. Remhof, Y.-S. Lee, Y. Yan, M.-Y. Kim, S. J. Kim, A. Züttel and Y. W. Cho, Thermal properties of $Y(BH_4)_3$ synthesized via two different methods, *Int. J. Hydrogen Energy*, 2013, **38**, 9263–9270.

23 J. E. Olsen, C. Frommen, T. R. Jensen, M. D. Riktor, M. H. Sørby and B. C. Hauback, Structure and thermal properties of composites with RE-borohydrides (RE = La, Ce, Pr, Nd, Sm, Eu, Gd, Tb, Er, Yb or Lu) and $LiBH_4$, *RSC Adv.*, 2014, **4**, 1570–1582.

24 M. Sharma, E. Didelot, A. Spyratou, L. M. Lawson Daku, R. Černý and H. Hagemann, Halide Free $M(BH_4)_2$ (M = Sr, Ba, and Eu) Synthesis, Structure, and Decomposition, *Inorg. Chem.*, 2016, **55**, 7090–7097.

25 M. Paskevicius, D. A. Sheppard, K. Williamson and C. E. Buckley, Metal hydride thermal heat storage prototype for concentrating solar thermal power, *Energy*, 2015, **88**, 469–477.

26 J. C. Crivello, R. V. Denys, M. Dornheim, M. Felderhoff, D. M. Grant, J. Huot, T. R. Jensen, P. de Jongh, M. Latroche, G. S. Walker, C. J. Webb and V. A. Yartys, Mg-

based compounds for hydrogen and energy storage, *Appl. Phys. A Mater. Sci. Process.*, 2016, **122**, 1–17.

27 M. B. Ley, D. B. Ravnsbæk, Y. Filinchuk, Y.-S. Lee, R. Janot, Y. W. Cho, J. Skibsted and T. R. Jensen, $LiCe(BH_4)_3Cl$, a New Lithium-Ion Conductor and Hydrogen Storage Material with Isolated Tetranuclear Anionic Clusters, *Chem. Mater.*, 2012, **24**, 1654–1663.

28 E. Roedern, Y.-S. Lee, M. B. Ley, K. Park, Y. W. Cho, J. Skibsted and T. R. Jensen, Solid state synthesis, structural characterization and ionic conductivity of bimetallic alkali-metal yttrium borohydrides $MY(BH_4)_4$ (M = Li and Na), *J. Mater. Chem. A*, 2016, **4**, 8793–8802.

29 Y.-S. Lee, M. B. Ley, T. R. Jensen and Y. W. Cho, Lithium Ion Disorder and Conduction Mechanism in $LiCe(BH_4)_3Cl$, *J. Phys. Chem. C*, 2016, **120**, 19035–19042.

30 M. B. Ley, S. Boulineau, Y. Filinchuk and T. R. Jensen, New Li Ion Conductors and Solid State Hydrogen Storage Materials: $LiM(BH_4)_3Cl$, M = La, Gd, *J. Phys. Chem. C*, 2012, **116**, 21267−21276.

31 S. P. GharibDoust, M. Brighi, Y. Sadikin, D. B. Ravnsbækb, R. Černý, T. R. Jensen and J. Skibsted, Synthesis, Structure and Li Ion Conductivity of $LiLa(BH_4)_3X$, X = Cl, Br, I, *J. Phys. Chem. C*, 2017, **121**, 19010–19021.

32 P. Schouwink, E. Didelot, Y.-S. Lee, T. Mazet and R. Černý, Structural and magnetocaloric properties of novel gadolinium borohydrides, *J. Alloys Compd.*, 2016, **664**, 378–384.

33 R. Černý and P. Schouwink, The crystal chemistry of inorganic metal borohydrides and their relation to metal oxides, *Struct. Sci. Cryst. Eng. Mater.*, 2015, **B71**, 619–640.

34 M. B. Ley, M. Jørgensen, R. Černý, Y. Filinchuk and T. R. Jensen, From $M(BH_4)_3$ (M = La , Ce) Borohydride Frameworks to Controllable Synthesis of Porous Hydrides and

Ion Conductors, *Inorg. Chem.*, 2016, **55**, 9748–9756.

35 J. E. Olsen, C. Frommen, M. H. Sørby and B. C. Hauback, Crystal structures and properties of solvent-free $LiYb(BH_4)_{4-x}Cl_x$, $Yb(BH_4)_3$ and $Yb(BH_4)_{2-x}Cl_x$, *RSC Adv.*, 2013, **3**, 10764–10774.

36 M. B. Ley, M. Paskevicius, P. Schouwink, B. Richter, D. Sheppard, C. E. Buckley and T. R. Jensen, Novel solvates $M(BH_4)_3S(CH_3)_2$ and properties of halide-free $M(BH_4)_3$ (M = Y or Gd)., *Dalton Trans.*, 2014, **43**, 13333–13342.

37 Y. Lee, J. Shim and Y. W. Cho, Polymorphism and Thermodynamics of $Y(BH_4)_3$ from First Principles, *J. Phys. Chem. C*, 2010, **114**, 12833–12837.

38 C. Frommen, N. Aliouane, S. Deledda, J. E. Fonneløp, H. Grove, K. Lieutenant, I. Llamas-Jansa, S. Sartori, M. H. Sørby and B. C. Hauback, Crystal structure, polymorphism, and thermal properties of yttrium borohydride $Y(BH_4)_3$, *J. Alloys Compd.*, 2010, **496**, 710–716.

39 W. Wegner, T. Jaroń and W. Grochala, Preparation of a series of lanthanide borohydrides and their thermal decomposition to refractory lanthanide borides, *J. Alloys Compd.*, 2018, **744**, 57–63.

40 V. Dyadkin, P. Pattison, V. Dmitriev and D. Chernyshov, A new multipurpose diffractometer PILATUS@SNBL, *J. Synchrotron Radiat.*, 2016, **23**, 825–829.

41 B. R. S. Hansen, K. T. Møller, M. Paskevicius, A.-C. Dippel, P. Walter, C. J. Webb, C. Pistidda, N. Bergemann, M. Dornheim, T. Klassen, J.-E. Jørgensen and T. R. Jensen, In situ X-ray diffraction environments for high-pressure reactions, *J. Appl. Cryst.*, 2015, **48**, 1234–1241.

42 K. T. Møller, B. R. S. Hansen, A.-C. Dippel, J.-E. Jørgensen and T. R. Jensen, Characterization of Gas-Solid Reactions using In Situ Powder X-ray Diffraction, *Zeitschrift für Anorg. und Allg. Chemie*, 2014, **640**, 3029–3043.

43 P. Fischer, G. Frey, M. Koch, M. Konnecke, V. Pomjakushin, J. Schefer, R. Thut, N. Schlumpf, R. Burge, U. Greuter, S. Bondt and E. Berruyer, High-resolution powder diffractometer HRPT for thermal neutrons at SINQ, *Phys. B Condens. Matter*, 2000, **276**–**278**, 146–147.

44 B. C. Hauback, H. Fjellvåg, O. Steinsvoll, K. Johansson, O. T. Buset and J. Jørgensen, The high resolution Powder Neutron Diffractometer PUS at the JEEP II reactor at Kjeller in Norway, *J. Neutron Res.*, 2000, **8**, 215–232.

45 T. Roisnel and J. Rodriguez-Carvajal, *'Computer program FULLPROF.' LLB-LCSIM*, 2003.

46 P. Giannozzi, S. Baroni, N. Bonini, M. Calandra, R. Car, C. Cavazzoni, D. Ceresoli, G. L. Chiarotti, M. Cococcioni, I. Dabo, A. D. Corso, S. Fabris, G. Fratesi, S. de Gironcoli, R. Gebauer, U. Gerstmann, C. Gougoussis, A. Kokalj, M. Lazzeri, L. Martin-Samos, N. Marzari, F. Mauri, R. Mazzarello, S. Paolini, A. Pasquarello, L. Paulatto, C. Sbraccia, S. Scandolo, G. Sclauzero, A. P. Seitsonen, A. Smogunov, P. Umari and R. M. Wentzcovitch, Quantum ESPRESSO: a modular and open-source software project for quantum simulations of materials, *J Phys Condens Matter*, 2009, **21**, 395502.

47 J. P. Perdew, K. Burke and M. Ernzerhof, Generalized gradient approximation made simple, *Phys. Rev. Lett.*, 1996, **77**, 3865–3868.

48 J. P. Perdew, Density-functional approximation for the correlation energy of the inhomogeneous electron gas, *Phys. Rev. B*, 1986, **33**, 8822–8824.

49 A. Otero-De-La-Roza and E. R. Johnson, Non-covalent interactions and thermochemistry using XDM-corrected hybrid and range-separated hybrid density functionals, *J. Chem. Phys.*, 2013, **138**, 204109.

50 A. Otero-de-la-Roza, E. R. Johnson and G. A. DiLabio, Halogen Bonding from

Dispersion-Corrected Density-Functional Theory: The Role of Delocalization Error, *J. Chem. Theory Comput.*, 2014, **10**, 5436–5447.

51 A. Wolczyk, E. R. Pinatel, M. R. Chierotti, C. Nervi, R. Gobetto and M. Baricco, Solid-state NMR and thermodynamic investigations on $LiBH_4$-$LiNH_2$ system, *Int. J. Hydrogen Energy*, 2016, **41**, 14475–14483.

52 H. J. Monkhorst and J. D. Pack, Special points for Brillouin-zone integrations, *Phys. Rev. B*, 1976, **13**, 5188–5192.

53 F. Franco, M. Baricco, M. R. Chierotti, R. Gobetto and C. Nervi, Coupling Solid-State NMR with GIPAW ab Initio Calculations in Metal Hydrides and Borohydrides, *J. Phys. Chem. C*, 2013, **117**, 9991–9998.

54 X. Zhang, Z. Wen, Z. Gu, X. Xu and Z. Lin, Synthesis and thermal behavior of the dawsonite-type solid solution $K_{1-x}(NH_4)_xAl(OH)_2CO_3$, *Thermochim. Acta*, 2005, **433**, 116–120.

55 A. R. West, *Solid state chemistry and its application, 2nd Edition*, 2014.

56 L. Hu, J. Chen, L. Fan, Y. Ren, Y. Rong, Z. Pan, J. Deng, R. Yu and X. Xing, Zero Thermal Expansion and Ferromagnetism in Cubic $Sc_{1-x}M_xF_3$ (M = Ga, Fe) over a Wide Temperature Range, *J. Am. Chem. Soc.*, 2014, **136**, 13566−13569.

57 L. Hu, J. Chen, A. Sanson, H. Wu, C. Guglieri Rodriguez, L. Olivi, Y. Ren, L. Fan, J. Deng and X. Xing, New Insights into the Negative Thermal Expansion: Direct Experimental Evidence for the ‘guitar-String’ Effect in Cubic ScF_3, *J. Am. Chem. Soc.*, 2016, **138**, 8320–8323.

58 R. D. Shannon, Revised effective ionic radii and systematic studies of interatomic distances in halides and chalcogenides, *Acta Crystallogr. Sect. A*, 1976, **32**, 751–767.

59 W. Wegner, T. Jaroń and W. Grochala, Polymorphism and hydrogen discharge from holmium borohydride, $Ho(BH_4)_3$, and $KHo(BH_4)_4$, *Int. J. Hydrogen Energy*, 2014, **39**,

20024–20030.

60 T. Sato, K. Miwa, Y. Nakamori, K. Ohoyama, H.-W. Li, T. Noritake, M. Aoki, S. Towata and S. Orimo, Experimental and computational studies on solvent-free rare-earth metal borohydrides $R(BH_4)_3$ (R=Y, Dy, and Gd), *Phys. Rev. B*, 2008, **77**, 104114.